Solid Freeform Fabrication 2023: Proceedings of the 34th Annual International Solid Freeform Fabrication Symposium – An Additive Manufacturing Conference
Reviewed Paper

Discovery of next-generation battery electrodes using topology optimisation

Chikwesiri Imediegwu[1,2*], Milo Shaffer[3], Mary Ryan[2], Ajit Panesar[1]

[1] IDEA Lab, Department of Aeronautics, Imperial College London SW7 2AZ
[2] Department of Materials, Imperial College London, SW7 2AZ
[3] Department of Chemistry, Imperial College London, SW7 2AZ

[*]Corresponding author:

Email: chikwesiri.imediegwu14@imperial.ac.uk

Abstract

Energy storage systems (ESSs) are essential components for the delivery of uninterrupted renewable energy of the future. A key stride towards the development of these systems revolves around the design of insertion-electrode batteries (IEBs). However, battery cell performance metrics of capacity and rate capability in these batteries are limited by inefficient ion and electron transport due to the complex transport channels the ions must navigate to reach storage sites – a fundamental limitation of slurry-cast (SC) type electrodes. We present a gradient-driven approach to derive optimal electrode architecture, constrained only by the underlying multiphysics system defining transport mechanisms in and across solid and liquid phases. The derived framework challenges the traditional manufacturing techniques for electrodes, inspiring novel strategies for deriving new high-performance electrodes.

Keywords: topology optimisation; nanoarchitecture; battery

Introduction

Efficient storage and deployment of renewable energy sources such as solar and wind energy are critical processes towards meeting the world's CO_2 reduction targets amidst increasing energy demand. Energy demand is expected to rise by 25% by the year 2030 [1]. The key challenge revolves around the fact these sustainable sources of energy are naturally intermittent - there exist no guarantees of meeting active energy demand on-the-fly. To harness and efficiently deliver these energy sources, large-scale storage systems are being developed to ‘even-out' delivery of these energy sources. A key component of such storage systems are batteries. Enhancing battery performance - capacity, rate capability, cycle efficiency and cycle life constitutes active research as scientists and engineers investigate improved battery materials and parameters [2,4].

IEBs such as lithium-ion (Li-ion) and sodium-ion (Na-ion) batteries represent recent technological advances in energy storage [1]. These batteries store chemical energy and supply electrical energy via mechanisms that feature shuttling ions between electrodes and electron movement in a loaded external circuit. Detailed descriptions of IEB cell mechanisms are well-documented in literature [1, 2]. Figure 1 shows an illustration of components and mechanisms within a typical insertion-electrode cell. Their electrochemical mechanisms depend on the ability

of some electrode materials to ingress or egress large quantities of lithium or sodium atoms without chemically changing the composition of the host material itself - diffusion mechanisms known as intercalation and de-intercalation respectively where atoms are inserted or removed from between the layers of the crystal structure of the host material. Traditional battery electrodes for these insertion-electrode cells consist mainly of active material particles and smaller quantities of conductive additives all held together by binding material. There exists a separation of scales of about one or two orders of magnitude between the electrode scale and the scale of the constituting particles. As a result, battery electrodes have been historically modelled as continuum scale structures. The classical Doyle-Fuller-Newman (DFN) framework [10, 14] is the most popular physics-based continuum scale description of electrochemical processes in insertion-electrode battery cells. The framework presents a means to simulate electrochemical phenomenon efficiently and accurately without the computational intricacies of particle electrochemical kinetics. Such a model accounts for the solid potential, electrolyte potential and ion concentration in the electrolyte in one spatial dimension while a radial `pseudo' dimension accounts for ion concentration in the electrode particles.

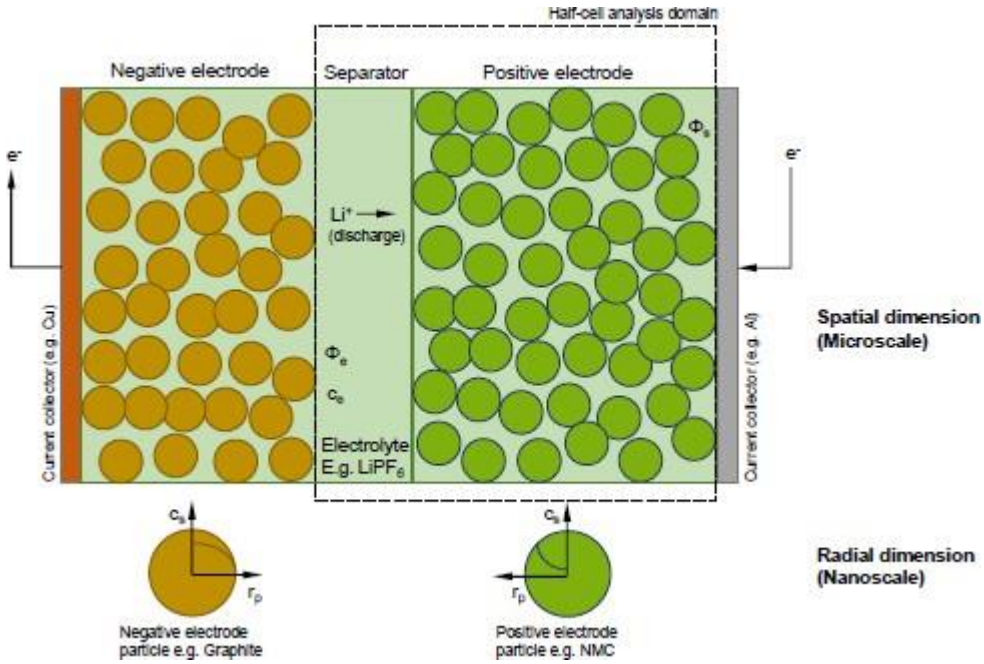

Figure 1: Illustration of DFN Li-ion cell configuration showing the direction of lithium ions during a discharge, state variables, the spatial and the radial dimensions. Particle kinetics are computed from the radial dimension. Both scales are coupled by particle surface kinetics. Binder and conductive additives have been excluded.

Some works to improve cell performance have featured optimisation of cell parameters such as separator and electrode thickness [4,5], active particle size [6] and particle distribution [7] often using a design of experiments to evaluate cell performance at discrete parameter values. This work presents a computational framework that leverages the underlying physics of ion and electron transport mechanisms to derive nanoscale topologies that optimise battery performance, specifically battery capacity and rate capability. The approach is superior to the pore engineering strategies mentioned above because it allows the physics phenomena to determine the best topology and size of architectural features of the electrode. The framework challenges classical electrode manufacturing techniques, opening the door to other advanced manufacturing strategies for realizing the physics-

informed electrode designs of our work.

Method

Continuum scale model

Consider a DFN electrode model that features a two-dimensional spatial dimension and a radial dimension for electrode particles (such as shown in Figure 1). Spherical particles of uniform particle size have been assumed. Also, only spherical symmetrical concentration distribution is allowed and convection in the electrolyte phase is assumed negligible. To model effective transport properties in this continuum scale, the Bruggeman's relations have been employed so that homogenized transport properties are derived as functions of penalized bulk transport properties of solid and electrolyte phases. Diffusion within the solid particles is assumed constant regardless of degree of lithiation. No mechanical or thermal considerations have been made. For completeness, the continuum scale battery modelling equations for insertion electrode batteries are briefly enumerated below and are based on conservation of charge and mass equations in the solid electrode active material (Equations (1) and (2) respectively) and the liquid electrolyte (Equations (3) and (4) respectively). Equation (5), known as the Butler-Volmer equation couples the system of equations across both phases by computing the lithium-ion flux across the solid-liquid interphase, ie. the solid particle surface.

$$\nabla.\left(-\mathrm{K_s^H}\nabla\Phi_\mathrm{s}\right) = -\mathrm{a_s j} \tag{1}$$

$$\frac{\partial \mathrm{c_s}}{\partial \mathrm{t}} = \frac{1}{\mathrm{r}^2}\frac{\partial}{\partial \mathrm{r}}\left(\mathrm{D_s r}^2\frac{\partial \mathrm{c_s}}{\partial \mathrm{r}}\right) \tag{2}$$

$$\nabla.\left(-\mathrm{K_e^H}\left[\nabla\Phi_\mathrm{e} - \frac{2\mathrm{RT}}{\mathrm{F}}(1-\mathrm{t}^+)\nabla \ln \mathrm{c_e}\right]\right) = \mathrm{a_s j} \tag{3}$$

$$\rho_\mathrm{e}\frac{\partial \mathrm{c_e}}{\partial \mathrm{t}} = \nabla.\left(-D_e^H\nabla \mathrm{c_e} + \frac{\mathbf{i}_\mathrm{e}^\mathrm{H}\mathrm{t}^+}{\mathrm{F}}\right) + \frac{\mathrm{a_s j}}{F} \tag{4}$$

$$\mathrm{j} = \mathrm{i_o}\left[\exp\left(\frac{(1-\beta)\mathrm{F}\eta}{\mathrm{RT}}\right) - \exp\left(-\frac{\beta \mathrm{F}\eta}{\mathrm{RT}}\right)\right] \tag{5}$$

Full derivations of these ion and electron transport equations can be found in literature [2]. All parameters and variables used in the numerical formulation are summarized in Table 1.

Parameter	Symbol	Value
Active materials (NMC622)		
Particle radius	r_p	4 μm
Diffusion coefficient	D_s	$2 \times 10^{-13} m^2 s^{-1}$
Bulk electronic conductivity	K_s	10 S m^{-1}
Max lithium concentration	$c_{s,max}$	47664 mol m^{-3}
Li-ion transference number	t^+	0.38
Initial state-of-charge	SOC_i	0.258
Final state-of-charge	SOC_f	0.95

Global volume fraction	ρ_s	$\int_{\Omega} \rho_\gamma \, d\Omega$
Electrolyte (LiPF6)		
Bulk diffusion coefficient	D_e	$7.5 \times 10^{-11} m^2 s^{-1}$
Initial lithium concentration	c_{in}	$1000 \text{ mol } m^{-3}$
Global volume fraction	ρ_e	$0.9 - \rho_s$
Reaction kinetic parameters		
Reaction rate constant	k	5×10^{-10}
Cathodic symmetry factor	β	0.5
Faraday constant	F	96485 Cmol^{-1}
Ideal gas constant	R	$8.314 \text{ JK}^{-1}\text{mol}^{-1}$
Temperature	T	298 K
Domain Dimensions		
Electrode thickness	L	60 μm
Separator thickness	L_{sep}	20 μm
Cell height	H	60 μm

Table 1: Summary of parameters and their values used for the battery cell continuum model evaluation

Homogenised transport properties in the continuum equations for electrolyte conductivity and diffusivity, K^H and D^H as well as the electrode conductivity, K^H are given by the Bruggeman relations:

$$\begin{aligned} K_e^H &= K_e(1-\rho_s)^{1.5} \\ K_s^H &= K_s\rho_s^{1.5} \\ D_e^H &= D_e(1-\rho_s)^{1.5} \end{aligned} \tag{6}$$

The specific active surface area is given as $a_s = \frac{3\rho_s}{r_p}$ with the cell overpotential given as: $\eta = \Phi_s - \Phi_e - E_{ocp}$, for which E_{ocp} is the open circuit potential for the cell. Finally, the exchange current density, i_0 is a function of the lithium concentration at the solid-electrolyte interface (surface of the active particles) given by:

$$i_0 = Fkc_{s,surf}^{\beta} c_e^{1-\beta} \left(c_{s,max} - c_{s,surf}\right)^{1-\beta} \tag{7}$$

Detailed derivations of the continuum equations enumerated here are available in literature [3]. These equations are solved numerically by a time-dependent solver on a discretized domain for the solid and electrolyte phase potentials, Φ_s and Φ_e, the solid and electrolyte phase lithium-ion concentrations, c_s and c_e, as well as the flux transfer kinetics at the solid-electrolyte interface, j.

Model Evaluation

The half-cell continuum model derived using Equations 1-7 above and parameter values of Table 1 was evaluated by applying discharge current, $I_D = 30C_{rate}$ A m^{-2} at C-rates 0.1C, 1C, 3C, 5C and 10C as shown in Figure 2. The battery cell was discharged over the time interval T_i to T_f. The final time, T_f was not explicitly defined but corresponded to a preset cut-off voltage of 3.33V.

Battery performance was evaluated as the Energy density, W, given as:

$$W = \int_{T_i}^{T_f} I_D V_D \, dT \tag{8}$$

where V_D represents the voltage profile during the discharge process. The results show performance peaks at different global volume fractions for each discharge rate. At low C-rates, the performance is monotonic – always increasing as the volume fraction of active material increases. However, as the discharge rate is increased, the performance is limited, reaching a peak value, and deteriorating despite further increasing active material volume fraction. Beyond the peaks, material utilization deteriorates suggesting inefficient ion transport to storage sites. To improve battery cell performance, capacity as well as rate capability must be improved. Active material volume fraction and indeed electrode microarchitecture is critical to cell performance. This limitation on cell performance provides inspiration for this work.

This work aims to improve cell performance (capacity and rate capability), by improving the efficiency of ion transport mechanisms to storage sites. Rather than determining a global volume fraction, ρ_s which maximizes cell performance, we allow the underlying ion transport phenomenon control the volume fraction of active material locally by setting up an optimisation problem with the objective of maximizing cell performance. By determining the sensitivity of the performance metric to the local design variables, a gradient-based optimisation search is derived. The outcome of the search corresponds to the optimal layout of active material which facilitates ion and electron transport to maximize the battery cell's performance. A mathematical formulation of such an optimisation problem follows.

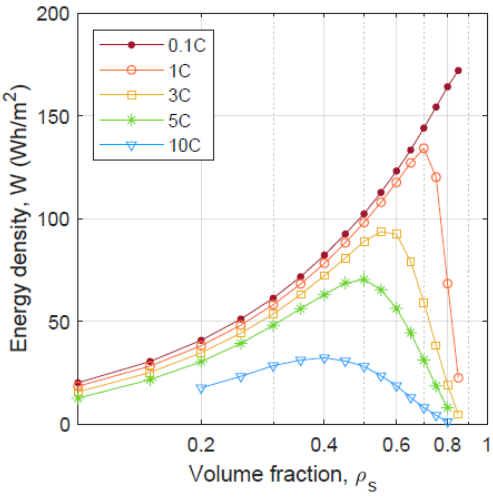

Figure 2: Variation of areal energy density with active material volume fraction for different C-rates. Plot shows performance peaks at different active material volume fractions for each discharge rate.

Optimisation Problem Formulation

Having established a numerical continuum model for which cell performance can be evaluated given a discharge current, we formulate an optimisation problem to maximize energy density for the discharge process. Mathematically, the problem is formulated by:

$$\text{maximize:} \quad W(\mathbf{U}(\rho_\gamma), \rho_\gamma)$$

$$\text{subjectto:} \quad F(\mathbf{U}(\rho_\gamma), \rho_\gamma) = 0$$

$$0 \le \int_\Omega \rho_\gamma(\mathbf{x}) d\Omega \le \rho_s$$

$$\rho_L \le \rho_\gamma(\mathbf{x}) \le \rho_U$$

where the solution vector, **U** consists of all the variables solved for as described in the continuum model formulation and ρ_γ is the local volume fraction of active material – a function of spatial coordinates which serves as the optimisation control variables. The search is constrained by the system of equations governing ion and electron transport. The control variables are bounded locally so that the active material volume fraction lies between $\rho_L = 0.01$ and $\rho_U = 0.9$. Conductive additives and binder material is assumed to occupy 10% locally and the rest of the space is occupied by electrolyte. The global volume fraction, $\rho_s = 0.6$ is set so that at optimisation initialization, ρ_γ is 0.6 everywhere. The global volume fraction is constrained during the optimisation. The real-valued objective functional, W, depends on the solution vector, $\boldsymbol{U}$. It also depends on the vector of control variables, ρ_γ. Sensitivities of the objective to the control variables have been determined by the adjoint method. Optimisation termination occurs when the objective value converges within a tolerance of 10^{-4} or the maximum number of iterations is reached.

Results and Discussion

Figure 3 shows the optimal layout of the electrode active material volume fraction at optimisation termination. The solution shows that cell performance is maximized when ion and electron transport is facilitated to all regions of the domain. Channels consisting of electrolyte project into the electrode domain towards to the current collector side, creating layers of dense electrode material.

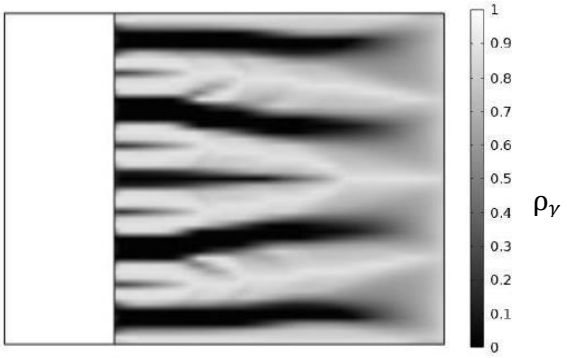

Figure 3: Optimised electrode topology described by optimal layout of the local volume fraction of active materials. Dark regions are predominantly electrolyte and the white regions indicate active material of highest volume fraction. The grey regions are regions of porous electrode material with intermediate volume fraction.

The paths taken by Li-ions into the electrode are plotted in the streamlines of Figure 4. Regions of tightly packed streamlines indicate preference for electrolyte phase transport as the Li-ions travel to regions of previously poorly utilized active material. With the homogeneous SC type electrode, these regions were difficult to be reached by ions due to the effective tortuous random channels available for electrolyte percolation. The streams lines can be observed to bend as the Li-ions intercalate into the active materials layers.

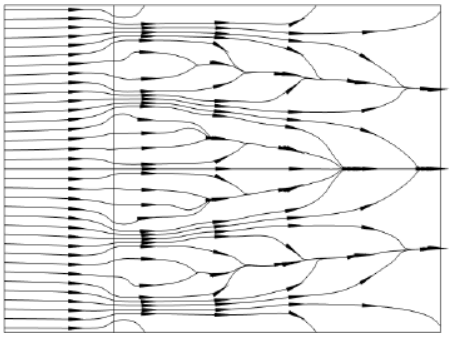

Figure 4: Lithium-ion flux streamlines, originating from the negative electrode surface, travel across the separator into the optimised continuum layout of active materials

The optimised electrode also offers an increased depth of discharge at cutoff voltage which terminates the cell discharge as shown in Figure 6a. At 5C discharge rate, the optimised electrode offers 15.4% increase in areal capacity compared to the uniform electrode at cutoff voltage.

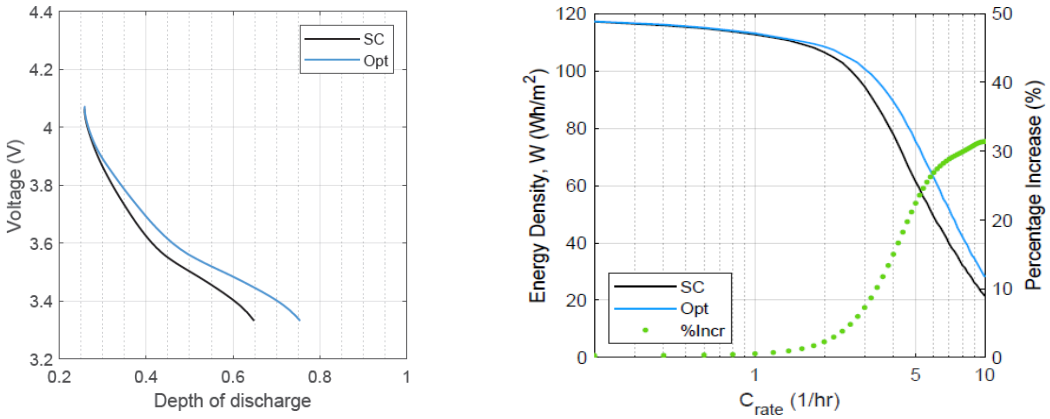

Figure 5: (a) Depth of discharge into positive electrode at 5C discharge rate for SC and Optimised electrodes. (b) Energy density at different C-rates for SC and optimised electrodes, showing performance increase at different C-rates (green dotted markers).

The improvement in cell performance is shown in Figure 6(b) where the variation of energy density achieved at discharge termination is compared for both electrodes for a range of discharge rates. It can be observed that there is a 22.4% increase in energy density when the optimised electrode is discharged over the uniform electrode at 5C discharge rate. The variation of gains in performance for different C-rates also shows that at low C-rates (below 1C), the optimised electrode offered no significant advantage in performance. This is consistent with observations of other works since discharge at low current density provides sufficient time for lithiation throughout the electrode domain, regardless of electrode architecture. Hence, the benefits of an optimised electrode topology increase with discharge rates as uniform electrodes suffer deteriorating rate capability and material utilization. In the range 3C to 5C, the percentage increase in performance is most sensitive to C-rate suggesting a practical range for use during gradient-based optimisation formulations involving time-dependent discharge process.

Summary and Conclusion

A continuum scale P3D model was developed according to established continuum equations describing ion and electron transport in and across solid and electrolyte phases. The model was evaluated at a range of C-rates and active material volume fractions to highlight the significance of active material layout to cell performance. By mathematically formulating an optimisation problem, the energy density of the electrode was maximized by controlling local volume fraction of the electrode material. The result was the generation of optimal layout of electrode material for maximizing the cell performance. The optimal topology was shown to facilitate ion transport to hitherto under-utilized regions of the electrode domain. Most importantly, the optimised electrode offered over 15% increase in areal capacity and over 22% increase in areal energy density when discharged at 5C discharge rate. Further improvements in performance were attained for higher C-rates. This work demonstrates that physics-informed computational optimisation can identify optimal electrode topology for efficient ion and electron transport, maximizing battery performance.

In future works, model fidelity will be enhanced to support a more robust cell performance optimisation by coupling diffusion and stress to state of charge. Proposed architectures will be tested experimentally using these patterned electrodes.

Acknowledgement

The authors acknowledge the funding support of Shell and the contributions of Peter Klusener, Magda Titirici, Ifan Stephens and all other collaborators on the NanoBat project.

References

[1] Plett G.L. Battery Management Systems: Battery Modelling, 2015

[2] Gupta A., Seo J.H., Zhang X., Du W., Sastry M.A., Shyy W. Effective transport properties of Lithium Manganese Oxide Electrode via Particle-Scale Modeling. Journal of the Electrochemical Society, 2011(158)5: A487-A497

[3] Wood D.L., Li J., Daniel C. Prospects for reducing the processing cost of lithium ion Batteries. Journal of Power Sources (275):234-242

[4] Zhao R., Liu J., Gu J., The effects of electrode thickness on the electrochemical and thermal characteristics of lithium ion battery, Applied Energy 139 (2015)220-229

[5] Lee D.C., Lee K.J, Kim C.W., Optimisation of a lithium-ion battery for maximization of energy density with design of experiments and micro-genetic algorithm, Internal Journal of Precision Engineering and Manufacturing 7 (2019) 829-836

[6] Chen K.H., Namkoong M., Goel V., Yang C., Kazemiabnavi S., Mortuza S., Dasgupta, N., Efficient fast-charging of lithium ion batteries enabled by laser-patterned three-dimensional graphite anode architectures, Journal of Power Sources 471 (2020) 228475

[7] Luo Y., Huang, L., Liu J., Wang Z., Chen Q., Chen Y., The optimisation of porosity and particle size for micron-size porous silicon in high energy pre-lithiated silicon graphite composite for li-ion batteries, microporous and mesoporous materials 331 (2022) 111672.

[8] Deng C., Lu W., Geometry optimisation of porous electrode for lithium-ion batteries, ECS Transactions 97 (2020) 249-254.

[9] Roy T., Salazar de Troya M., Worsley M., Beck V., Topology optimisation for the design of porous electrodes, Structural and Multidisciplinary Optimisation 65 (2022) 1-21

[10] Doyle M., Fuller T., Newman J., Simulation and optimisation of the dual lithium ion insertion cell, Journal of the Electrochemical Society 141 (1994) 1-10

[11] Lu X., Bertei A., Finegan D., Tan C., Daemi S., Weaving J., O'Regan K., Heenan T., Hinds G., Kendrick E., Brett D., Shearing P., 3D microstructure design of lithium-ion battery electrodes assisted by x-ray nano-computed tomography and modelling, Nature Communications 11 (2020) 2079.

[12] Lu X., Zhang X., Tan C., Heenan T., Lagnoni M., O'Regan K., Daemi S., Bertei D., Shearing P., Multi-length scale microstructural design of lithium-ion battery electrodes for improved discharge rate performance, Energy Environmental Science, 14 (2021) 18624-18632

[13] Boyce A., Cumming D., Huang C., Zankowski S., Grant P., Brett D., Shearing P., Design of Scalable, Next-Generation Thick Electrodes: Opportunities and Challenges, 15 (2021) 18624-18632

[14] Doyle, M., Fuller T., Newman., Modelling of galvanostatic charge and discharge of the lithium/polymer insertion cell, Journal of the Electrochemical Society, 140 (6) 1526-1533